In Line Study of Droplet Deformation in Polymer Blends in Channel Flow

K. B. MIGLER, E. K. HOBBIE, *and* F. QIAO

Polymers Division
National Institute of Standards and Technology
Building 224, Room B210
Gaithersburg, Maryland 20899

We present *in situ* measurements of a dilute polymer blend in channel flow using an optical flow cell placed at the exit of a twin screw extruder. At weak shear stress, we find mildly deformed ellipsoidal droplets whereas at moderate shear rates we find coexistence between large aspect ratio strings and ellipsoidal droplets. In the regime of low to moderate stress, depth resolved optical microscopy reveals that the deformation is a function of local shear stress. At large shear stress, the droplet breakup is suppressed; mildly deformed droplets at high capillary number are observed, in contrast to the Taylor model. Optical light scattering provides complementary morphological information that is averaged over the channel depth and confirms the optical microscopy. We discuss these results in terms of Taylor theory and normal forces.

INTRODUCTION

The properties of a polymeric material can frequently be enhanced by blending it with a second immiscible polymer that contains synergistic properties (1, 2). For example, the blending of rubber into nylon can achieve a significant increase in impact strength (3). In other cases, the matrix can provide mechanical strength while the minor component provides a barrier to gas permeation (4). The final properties are quite sensitive to the quality of the dispersion. In the case of a nylon-rubber blend, a change in the average size of the minor particle from 0.48 μm to 1.59 μm results in a 50°C shift in the brittle-tough transition (5).

The development of new polymer blends systems will require precise control over the dispersion process. Unfortunately, the scientific understanding of dispersing polymeric materials still lags behind the technological capability to produce them. The standard model of droplet breakup is based on the pioneering works of Taylor and Tomatika (6–8) and has been the inspiration for numerous subsequent studies (9–14). In viscous media, there are two dimensionless parameters controlling stress-induced breakup of a droplet in a liquid matrix; the viscosity ratio and the capillary number. The viscosity ratio is defined as

$$\lambda = \frac{\eta_d}{\eta_c}, \tag{1}$$

where η_d and η_c are the viscosities of the drop and continuous phases respectively. The second parameter is the capillary number of a droplet in a shear field;

$$\mathrm{Ca} = \frac{\sigma R_o}{\kappa}, \tag{2}$$

where σ is the shear stress of the matrix phase, κ is the interfacial tension and R_o is the radius of the droplet (or cylinder). Ca measures the relative strength between the viscous stress σ, which tends to elongate the droplet, and the interfacial stress κ/R_o, which tends to make it circular.

There exists a critical capillary number $\mathrm{Ca_c}$ that defines a stability condition for a droplet in a flow field. For $\mathrm{Ca}/\mathrm{Ca_c} >> 1$, the viscous stress dominates the interfacial stress and the droplet deforms affinely with the shear flow. [In practice, affine deformation is observed for values of $\mathrm{Ca}/\mathrm{Ca_c}$ as low as two (15).] As the droplet elongates, its radius in the direction perpendicular to flow decreases, thus decreasing Ca. For $\mathrm{Ca}/\mathrm{Ca_c}$ slightly above one, the interfacial tension between droplet and matrix becomes important, causing a breakup of the elongated droplet into smaller droplets. If the smaller droplets have $\mathrm{Ca} < \mathrm{Ca_c}$, they will remain stable. $\mathrm{Ca_c}$ is a function of both λ and the type of flow (extensional or shear). For $\lambda > 4$ in simple shear flow, $\mathrm{Ca_c} \rightarrow \infty$ and droplet breakup is not observed.

The viscoelastic nature of polymeric fluids greatly complicates the above picture of droplet deformation

and breakup. Important insights have been made by using a viscoelastic droplet with a Newtonian matrix or vice-versa in a well controlled shear field; the literature in this area was recently summarized by Varanasi *et al.* (16). Elmendorp and Maalcke found that elasticity in the droplet tends to stabilize it (inhibit deformation and breakup) whereas elasticity in the matrix tends to destabilize it. Varanasi *et al.* found that in the case of a viscoelastic drop in a Newtonian matrix, the maximum stable droplet size at a given shear rate is not inversely proportional to the shear rate, but levels off above a certain shear rate (17, 18).

Several attempts have been made to modify *Equation 2* to account for the effects of viscoelasticity (19–21). Van Oene suggested that a term proportional to the difference between the first normal stress difference of the droplet and matrix phases should be added to the interfacial tension (20). Sundararaj and Macosko modify the shear stress to include a term proportional to the normal force differences between two phases (21).

Previous work to examine the issue of droplet deformation and breakup in polymer blends has mostly centered on two approaches. The dominant method is to create dispersions during either batch or continuous mixing operations, quench the material, and analyze it with electron microscopy (20, 22–33). In some cases a minimum in observed size as a function of average shear rate (or energy input) has been found (21, 27). Typically, at high shear rates, the average droplet radius is above that predicted by the Taylor theory, even in the dilute case in which coalescence is insignificant. While this technique does produce very detailed images of the sample, there are drawbacks; it is conducted off-line, it samples a limited quantity of material, and there can be changes occurring in the sample before it is quenched. For fundamental work, the flow field is too complex as these devices employ a combination of shear and extensional flow. In a second class of work, well defined shear flows are generated in transparent devices such as couette cells or cone and plate; the morphology is then probed via microscopy (16, 18, 34, 35) and/or scattering and dichroism (36–40). Owing to viscoelastic instabilities, these devices are limited to low shear rates or to solutions.

In this work, we present on-line measurements of a model polymer blend system—polystyrene droplets in a polyethylene matrix—carried out in an optical flow cell situated at the exit of a twin screw extruder. We combine stroboscopic microscopy, optical light scattering and flow velocimetry to construct a picture of the deformation and breakup process. The key advantage of this approach is that it allows one to directly view deformation and breakup during actual polymer processing. Thus, conditions of high stress and shear, high pressure and temperature, and non-uniform flow are all present. The ability to work at high shear stress means that effects of shear thinning and normal stresses can be studied.

INSTRUMENTATION

Recently we reported the construction of an optical flow cell instrumented with both a stroboscopic microscope and an optical light scattering apparatus situated at the end of a twin screw extruder (41). This instrument represents the transfer of a technology originally developed for a transparent cone and plate (38–40). Gogos *et al.* have utilized microscopy alone in an optical flow cell at the exit of a modified twin screw extruder (34).

The microscopy can measure individual droplets down to about 1 μm, while the light scattering can extract averaged information from droplets as small as about 0.1 μm. Thus, the length scale of typical immiscible polymer blends is well matched with the capabilities of the instrument. Solid pellets or powder are premixed to the desired concentration and are fed into the extruder under either flood feed or starve feed conditions (in this study flood feeding was used). The material is melted, mixed and extruded under pressure through the adjustable height slit die. *Figure 1* shows two flush mounted sapphire windows in the slit die which provide the optical access for microscopy and the light scattering. The microscopy and the light scattering measures the plane containing the flow and

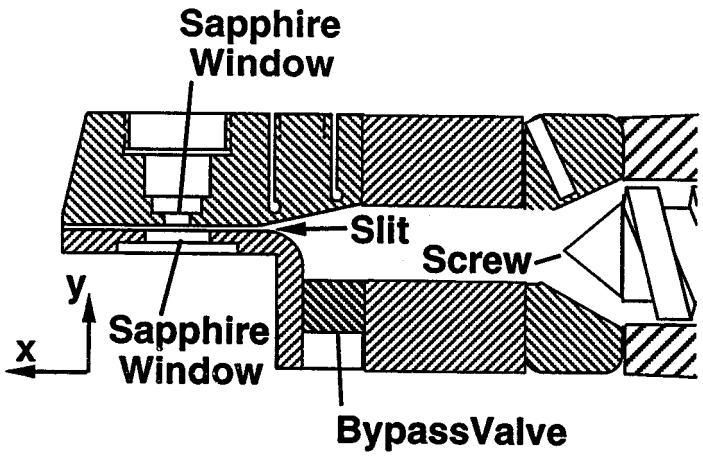

Fig. 1. Side view of the apparatus, showing the optical flow cell and the end tip of one of the screws. For the study of weak flow through the cell, the bypass valve is opened. In the slit die, the x, y, z directions are defined to be along the axes of the flow, the velocity gradient and the vorticity, respectively.

the vorticity (x-z). In this study, we used bright field illumination for the microscopy because the index of refraction of the two component polymers is large enough that phase contrast microscopy was not necessary. Translation of rail mounted optical components switches the configuration from micrcoscopy to light scattering (41). In this study, the length scales observed are in the range of (0.5 to 15) μm, for which both microscopy and light scattering studies can be carried out. When feasible, optical microscopy provides more information that is easier to interpret than light scattering, thus most of the work presented here will be from the microscopy. Light scattering becomes particularly useful at shorter length scales.

We can also use the microscope to conduct flow velocimetry measurements. By using a stroboscopic particle tracking technique, we can measure the velocity as a function of distance from the wall. In this work, we track dust and other impurities in the polymer. For measuring fast flows, the strobe is flashed twice per video frame where the time between flashes is adjustable and can be as short as 2 ms. With the width of a video image of 200 μm this allows measurement of velocities up to 10 cm/s. The depth resolution of the optics is approximately 40 μm, giving an ability to measure shear rates on the order of 10^3 s^{-1}.

The size of the droplets entering the slit die is controlled by the extrusion conditions (temperatures of processing zones, screw rotation rate, feed rate etc.). The melting, mixing and flow process within the twin screw extruder is quite complex. The flow is predominately shear in the extruder although it is elongational in the nip regions between the screws. In the region of the die just before the slit, the height of the channel narrows considerably, creating extensional flow.

The flow in the slit itself is shear flow. In this study we utilize the extruder as a device which prepares the dispersion and then pumps it at high pressure through the slit die. Our focus is on the effect of channel flow on the droplets that enter the die. Thus we observe the elongation and breakup of string-like droplets in the die caused by the shear flow. In order to ascertain that the shapes observed are due to the shear flow in the die, we occasionally stop the flow, allow all the droplets to become spherical, and then restart the flow. At short enough times, the observed droplets have only been in the slit die (not the contracting entrance region) since the restart of flow. By comparing the time it takes for the droplets to assume their steady state shape with the time that they have only been in the slit, we can state that the flow in the slit is responsible for the observed shape.

For the particular blend system used here, typical sizes of the dispersed droplets are on the order of 1 μm, which is at the lower limit of the observing powers of the microscope. Hence morphology can be visualized, in particular the elongation into strings, but the diameter of strings and the resulting drops cannot be accurately measured.

RHEOLOGY

In this work, the matrix phase was a high density polyethylene (HDPE) Dow no. 08454N, and the droplet phase was Dow Polystyrene 612 (42). Rheological measurements were carried out using two methods. For dynamic shear and low steady state shear, we used a plate—plate device (Rheometrics ARES). For the high shear regime, we use the optical slit die as a rheometer —we measure flow rate as a function of shear stress at the wall. A single pressure transducer located shortly after the extruder screws is used for the pressure gradient measurement. Although we cannot make entrance pressure corrections, the advantage of this technique is that we conduct rheological measurements under the same conditions that are found in the experiment. Thus issues of shear heating, flow degradation and pressure corrections are minimized. The shear stress and the flow rate at the wall are calculated by standard rheological methods (43). The shear stress at the wall is controlled by adjusting the rotation rate of the screws (flood feed conditions), which of course also changes the overall pressure drop across the slit and the material throughput. *Figure 2* shows the results taken at 195°C. At low shear rates, the polystyrene is approximately 2 times more viscous than the polyethylene. At higher shear rates, the rheology is fit to a power law model

$$\eta(\dot{\gamma}) = K\,|\dot{\gamma}|^{n-1}; \tag{3}$$

where K is the consistency index, n the power law index and $\dot{\gamma}$ is the shear rate. For PE and PS $n = 0.68 \pm 0.02$ and $n = 0.39 \pm 0.02$, respectively, with the expanded uncertainty based on a fit to the data. Because of the more pronounced shear thinning by the polystyrene, its viscosity equals or is less than that of the polyethylene at the largest shear rates.

In *Figure 2B*, we measure the normal force combination $N = N_1 - N_2 \approx N_1$ for these two polymers in a parallel plate device. When plotted as a function of shear stress, the PE exceeds that of the PS at low stress. However, the difference between the two narrows as stress increases, and extrapolation of the data yields a crossover at higher shear stress where the normal force of the PS (droplets) exceeds that of the PE (matrix).

As discussed in the **Introduction**, a controlling parameter for droplet breakup is the viscosity ratio λ. While this is a well-defined quantity for small molecule liquids, one must be careful in applying this concept to shear thinning materials because one must know the shear rate (or shear rate distribution) within the droplet and compare that viscosity to that of the matrix. Furthermore, the shear (or stress) on a fluid element in the droplet is not constant in time, thus the concept of using a steady state shear viscosity to model the droplet may not be correct.

FLOW VELOCIMETRY

In a slit die, the flow is parabolic when the highest shear rates are in the Newtonian regime whereas for

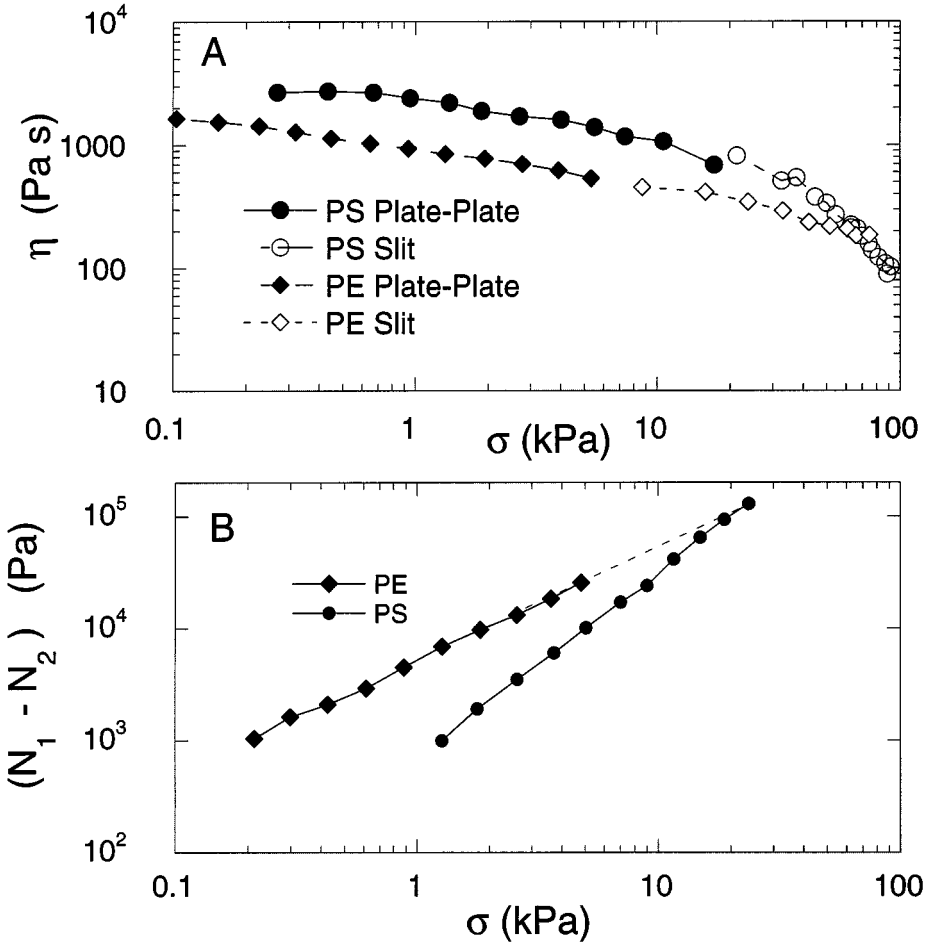

Fig. 2. A) Steady state viscosity of the polyethylene and polystyrene as a function of shear stress (T = 195°C). The low shear data was obtained in a plate-plate while the high shear data was generated by using the optical flow cell as a capillary slit rheometer. B) Normal force data taken with the plate-plate geometry as a function of shear stress (T = 195°C). The relative expanded uncertainty in the viscosity measurement is 15%, based on repeated measurements. The relative expanded uncertainty in the shear rate for the slit capillary data is also 15%, based on repeated measurements.

strong shear thinning, the flow becomes more plug like. In both cases, shear is greatest at the walls and decreases monotonically to zero as a function of distance to the center. Thus, we may reasonably expect that the deformation is a function of position from the wall. In order to understand the variation of blend morphology with depth, we first present measurements of the flow profile of the matrix phase as a function of shear stress at the wall. *Figure 3* shows measurements of the velocity of the PE as a function of depth from one wall to the center of the die for three representative flow rates. The measured flow at the wall is always greater than zero because one is observing a finite sized particle which feels a net force. However, the magnitude of this velocity is small enough that slippage is either absent or extremely small; thus we can use a no-slip approximation. The resulting data is fit to the curve

$$v(y) = v_0\left[1 - \left\{\left|\frac{y - d_o/2}{d_o/2}\right|\right\}^{\alpha}\right] \qquad (4)$$

where y is the vertical position (measured from the mid-plane), d_o is the height of the slit, v_0 is the velocity at the mid-plane, and α is related to the power law index n via $\alpha = 1 + 1/n$. The fluid profile at the lowest shear stress is Newtonian as indicated by a value of $\alpha = 1.9 \pm 0.1$. At the highest shear rate, $\alpha = 2.57 \pm 0.15$, which then corresponds to a power law index $n = 0.64 \pm 0.06$, (expanded uncertainty based on the results of a fit to the data), consistent with the value found from capillary slit die measurements. This level of shear thinning is relatively modest with considerable shear occurring over most the sample. [For a counter example, see (41), which shows the flow profile of the PS.]

MORPHOLOGY NEAR CRITICAL CAPILLARY NUMBER

Capillary breakup is directly observed via optical microscopy by measuring the transition from ellipsoidal droplets to strings. We conduct these measurements in the immediate vicinity of the bottom wall. *Figure 4* is a sequence of video micrographs taken at increasing shear stress. The average size of these droplets is approximately 1 μm. In order to access this low shear rate regime needed to study breakup, the bypass valve is opened. At a wall shear stress $\sigma_w = (2.5 \pm 0.3)$ kPa shown in *Figure 4A*, the droplets are mildly elliptical, with aspect ratio below 2. (The relative expanded uncertainty in σ_w is ≈10 % and is due primarily to fluctuations in the pressure as measured by the pressure transducer past the screws.)

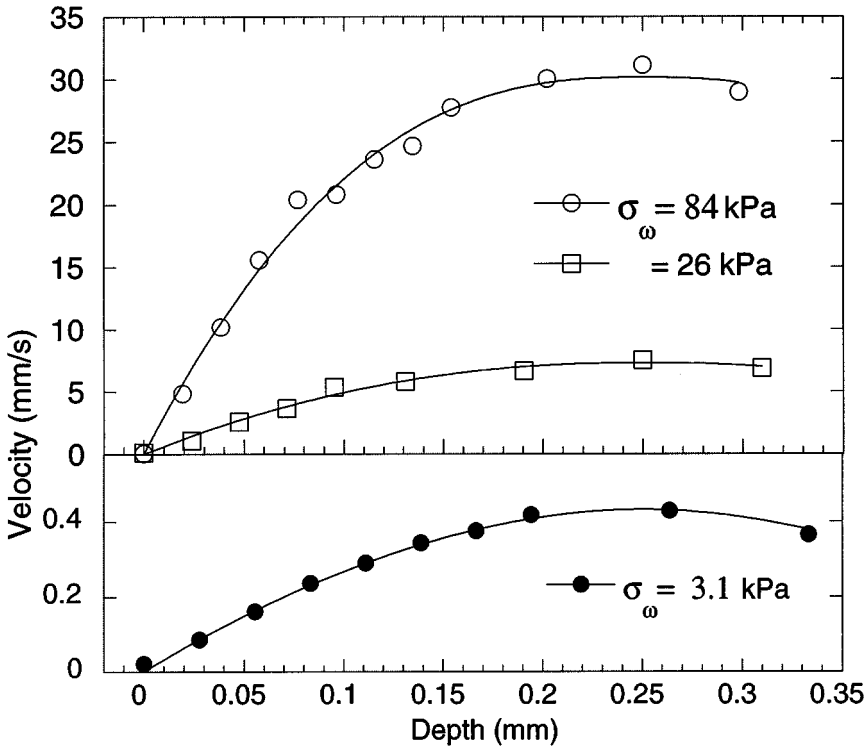

Fig. 3. Velocity profile measurements of the pure polyethylene for increasing wall shear stress. The relative expanded uncertainty in the velocity measurement is 7%, based on repeated measurements. The expanded uncertainty in the depth measurement is 0.01 mm, based on the resolution of the depth of focus.

Upon increasing the shear stress to σ_w = (3.4 ± 0.3) kPa (*Figure 4B*) we see that the largest droplets elongate greatly into strings. At this shear stress, we do not see evidence of the breakup of these elongated droplets, once formed they simply translate downstream at constant length. At a shear stress σ_w = (8.3 ± 0.8) kPa (*Figure 4C*), breakup of the largest strings is now observed. *Figure 4C* shows three strings near the center of the image that had been one long string. *Figures 4B* and *C* indicate that there may be a narrow region in shear stress in which the strings are stable. At still higher shear stress, most of the droplets have elongated into strings and the system can be described as a superposition of strings and mildly deformed ellipsoidal droplets. To estimate the critical capillary number, we use a droplet size of R_0 = 2 μm (estimated from the optical microscopy), shear stress σ = 2.5 kPa (estimated from the largest shear stress which did not produce strings) and interfacial tension κ = mN (44). Inserting these values into *Equation 2*

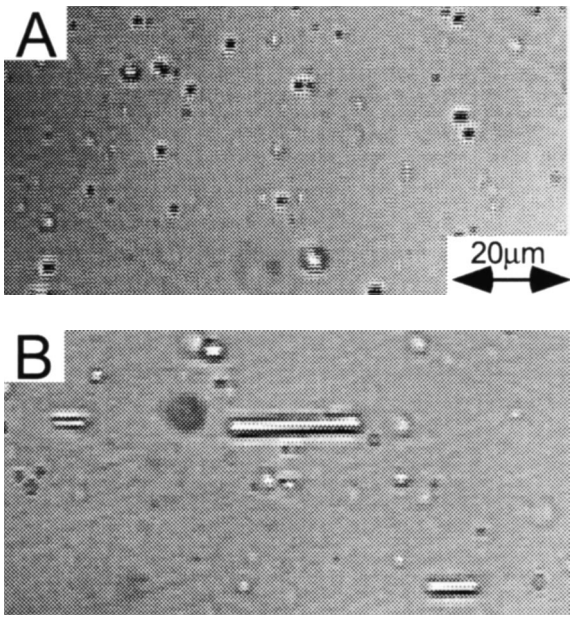

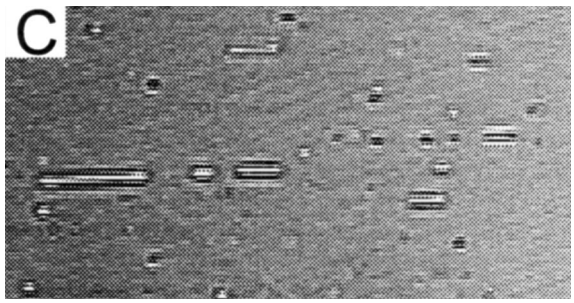

Fig. 4. Optical microscopy images of droplet deformation at the bottom wall in the regime of low shear stress. The transition from ellipsoidal to supercritical strings is a measure of the critical capillary number. A: σ_w = (2.6 ± 0.3) kPa, B: σ_w = (3.4 ± 0.3) kPa, C: σ_w = (8.3 ± 0.8) kPa.

yields the reasonable value of $Ca_c = 1$. In the above measurements, the point of observation (the bottom wall) was kept constant and the shear stress at the wall was increased by varying the overall pressure drop across the slit. Alternatively, one can hold the overall pressure drop constant and scan the point of observation from the wall to the center of the die. The shear stress is a maximum at the wall and decreases linearly to zero at the center of the die. It is therefore interesting to study the variation in droplet morphology with depth.

In *Figure 5*, we present typical images at four depths from the bottom wall. The shear stress at the wall is set so that the larger droplets are slightly above their critical capillary radius. The depth of the slit is $d_o = (0.5 \pm 0.5)$ mm (± is the expanded uncertainty) and these images scan from 0 mm $< d <$ 0.21 mm where d is the distance from the bottom wall. In *Figure 5A* (bottom wall), we observe a coexistence of elongated strings and ellipsoidal droplets. Some of the strings were clearly part of a longer extended string that broke up because of an instability. The sequence of strings across the middle of *Figure 5A* were part of a string that was (0.8 ± 0.1) mm long (expanded uncertainty). Thus before breakup it had an aspect ratio on the order of 10^3. As the distance from the wall is increased to (0.08 ± 0.1) mm, we still observe elongated strings, but we do not observe any evidence of their breakup. Thus at this shear rate, the lifetime of the strings exceeds the observation time of the experiment. At greater distances, the number density and aspect ratio of the strings declines, until the droplets are nearly spherical at a distance of (0.21 ± 0.1) mm.

In comparing the morphology at the wall as a function of shear stress (*Figure 4)* with that as a function of depth (*Figure 5*), we conclude that the local shear stress is the controlling parameter. Both show a transition from ellipsoidal droplets to strings at a shear stress of $\sigma = (2.5 \pm 0.3)$ kPa, and a capillary instability within the strings at a shear stress above 4 kPa. This indicates that the droplet size distribution is constant as a function of distance from the wall. Additionally, from *Figure 4C* and *Figure 5A* we can conclude that the mechanism for droplet breakup is from one long string into an irregular sequence of shorter strings. The diameters of the sequence of shorter strings is greater than that of the original string. This can be deduced form volume conservation as there is always a finite distance between the shorter strings that have broken up. This breakup mechanism is very different from what we observe when the shear is suddenly turned off; in that case a regular sequence of spherical droplets is formed with constant size and spacing, except for the last droplet at each end which is larger.

DROPLET MORPHOLOGY AT HIGH STRESS

When the shear stress is increased into the range that is typical of polymer processing, we observe an interesting sequence of morphologies. *Figure 6* shows the

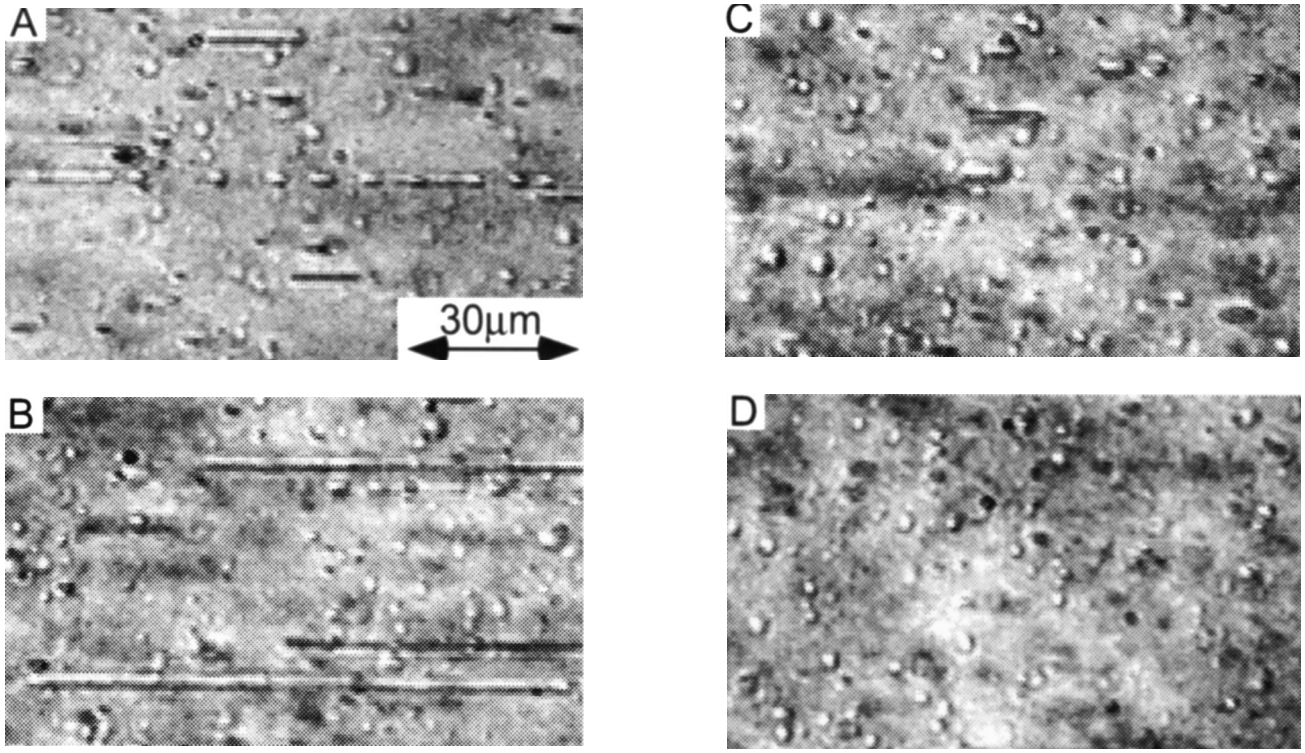

Fig. 5. Optical microscopy images of the droplet deformation as a function of depth from the bottom wall for the modest shear stress of $\sigma_w = (4.0 \pm 0.4)$ kPa. A: D = (0.0 ± 0.1) mm. B: D = (0.08 ± 0.02) mm. C: D = (0.16 ± 0.1) mm. D: D = (0.21 ± 0.1) mm. The total thickness is d = 0.5 mm.

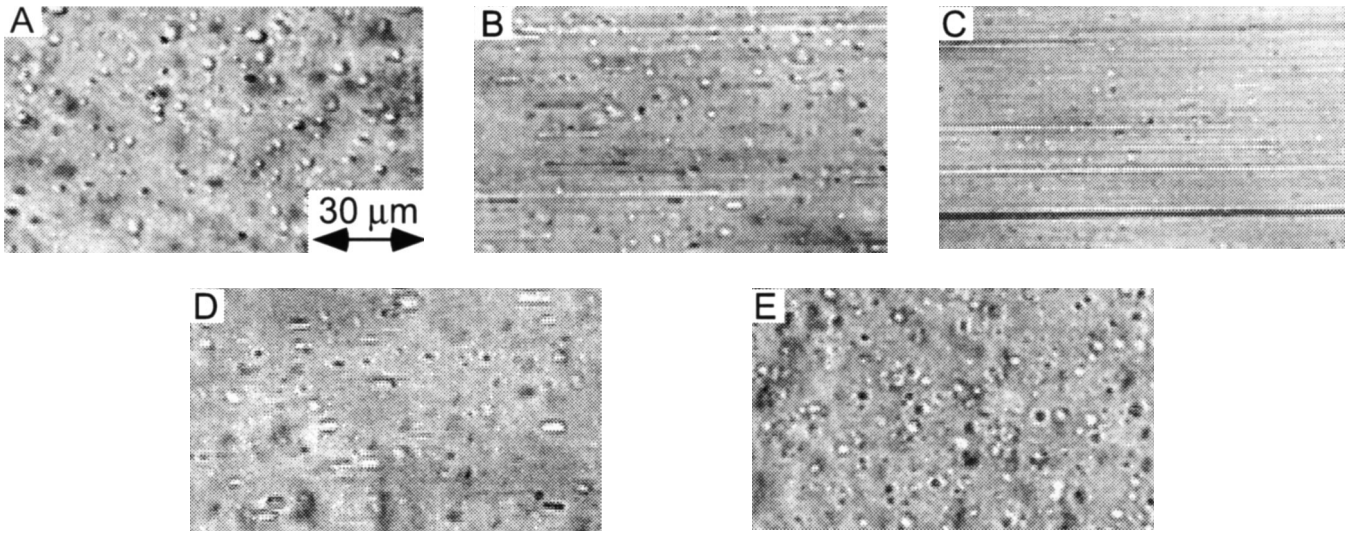

Fig. 6. Optical microscopy of the deformation as a function of wall shear stress for a depth of (0.08 ± .01) mm from the bottom wall demonstrating the transitions from ellipsoids to strings and back to ellipsoids. A: Ellipsoidal droplets at low shear stress, σ = (1.5 ± 0.2) kPa. B: Coexistence of droplets and strings σ = (11 ± 1) kPa. C: σ = (18 ± 2) kPa. D: σ = (44 ± 5) kPa. E: Return to the ellipsoidal morphology. σ = (64 ± 6) kPa.

observed morphologies as the shear stress is increased at a constant distance of mm from the bottom wall (~1/3 of the distance from wall to center of channel.) *Figures 6A* and *6B*, where and respectively, are typical of what was observed previously, i.e. a transition from ellipsoidal droplets to a coexistence of strings and ellipsoidal droplets. In *Figure 6C*, again there is a coexistence, but there is a shift in the distribution; the majority of observed droplets are string-like. As we move to higher shear stress, *Figures 6D* and 6*E*, where σ = (44 ± 5) kPa and σ = (64 ± 6) kPa respectively, a remarkable transition occurs; the droplets become ellipsoidal again, the string-like behavior disappears.

The conventional explanation for this effect is that the strings break up by a capillary instability before the point of observation; the droplets observed are below the critical capillary number and therefore strings are not observed. This breakup could occur either somewhere upstream (screw region or entrance region) or even in the slit itself but before the point of measurement. In addition to droplet breakup, there is evidence of an additional mechanism; the suppression of droplet elongation at high shear stress. *Figures 6A* and *6E* show similar droplet size distribution and density. If the droplet radius were two times smaller, for example, then the density would be increased by eight, which is clearly not observed. Additionally, the light scattering (see next section) indicates that the radius of the droplets in *Figures 6A* and *6E* are similar. The capillary number for a droplet 1 μm at the shear stress of *Figure 6E* (σ = 64 kPa) is thus Ca = 13, which is well above the critical capillary number as determined at low shear. Only weak droplet deformation is observed at this high capillary number, even though it was observed at low shear rates at a capillary number of 1. Additionally, at the highest shear stresses near the wall, the droplets align in the direction of the vorticity axis; this phenomena will be presented separately (45).

MORPHOLOGY DIAGRAM

We construct a morphology diagram as a function of depth and local shear stress which summarizes a series of depth dependent morphological measurements of the type presented in *Figures 4–6*. These were taken over a range of wall shear stress 1 kPa < σ_w < 80 kPa. The points along each diagonal solid line correspond to morphological measurements of the type shown in *Figure 5* and in which the flow rate was held constant and the microscope focus is scanned from the wall (d = 0) to the mid-plane (d = 0.25 mm). At the center the shear stress is zero, so that all lines converge to σ(d = 0.25 mm) = 0, whereas at the wall σ(d = 0) = σ_w. The morphology observed at a given depth and local shear stress is indicated by the type of data marker (circle or triangle). The data from one solid line to another at the same d corresponds to the type of experiment shown in *Figures 4* and *6*.

At low flow rates (*Figure 7A*), we observe the capillary breakup transition at σ = (2.5 ± 0.3) kPa described in the previous section. The horizontal dashed line separates the ellipsoidal droplets from the string-like droplets. The fact that this line is horizontal indicates that local stress is the controlling parameter.

At higher flow rates, there are two important features in the data. First, for all flow rates, the morphology is elliptical (actually spherical) at the midplane (d = 0.25 mm). This indicates that the local shear, which is zero, controls the morphology, rather than the upstream flow. The second feature in this diagram is that away from the mid-plane we see the transition from strings and ellipsoids back to ellipsoids as the flow rate is increased, as seen in *Figure 6*. Moreover,

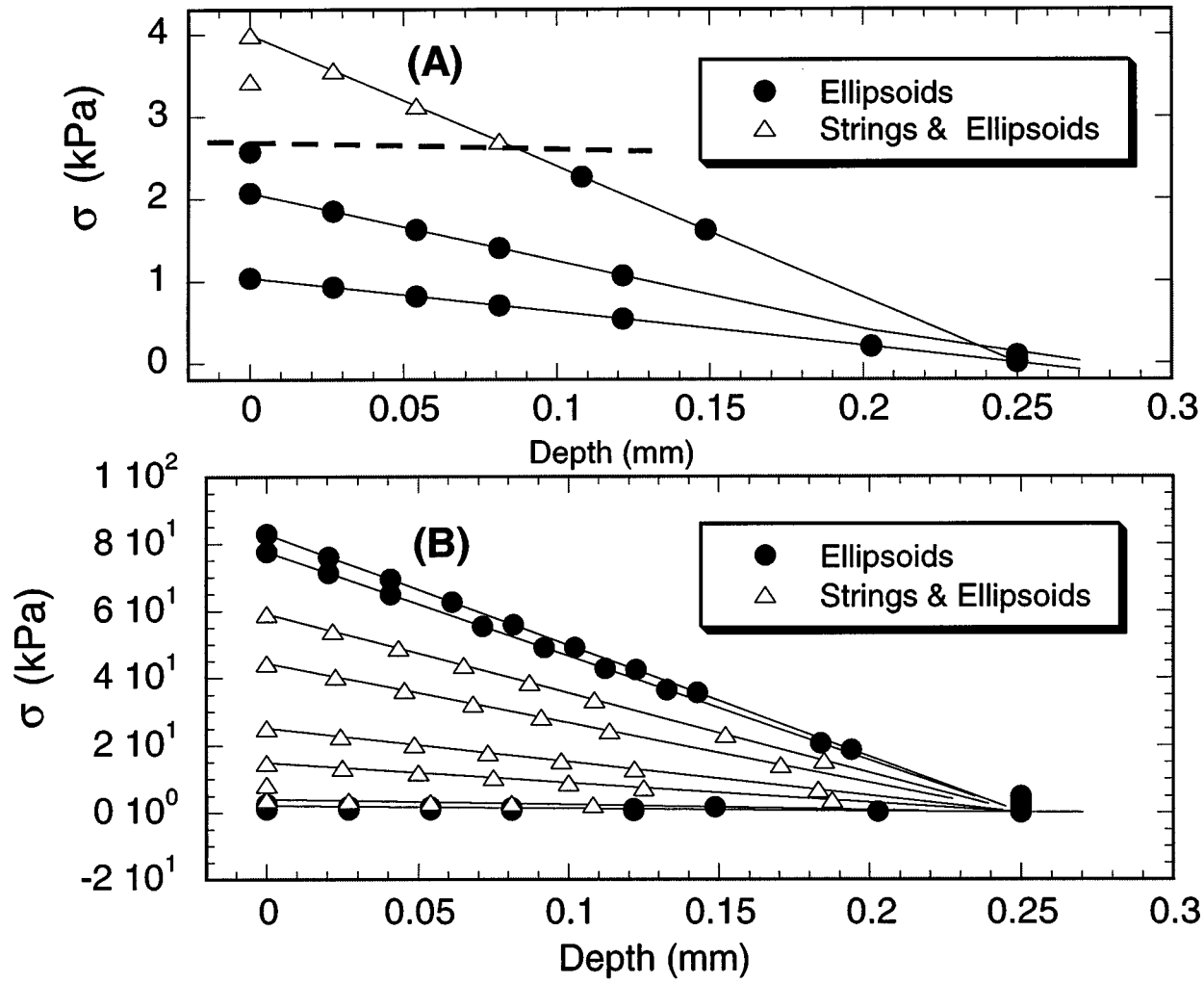

Fig. 7. State diagram of droplet morphology as a function of local shear stress and position. Points connected along a solid line correspond to the same σ_w, that is, the point of observation is scanned while the RPM and fluid flow rate are held constant. A: At low shear stress, the dotted line separates ellipsoidal droplets from a coexistence of ellipsoids and strings, indicating that local shear stress is the controlling parameter for morphology. B: The dashed line indicates the return to ellipsoidal morphology at high shear stress.

the transition is dependent on the overall flow rate (or pressure drop), rather than the local shear stress. As mentioned above, at the highest shear stresses near the wall, the droplets align in the direction of the vorticity axis (45).

LIGHT SCATTERING

Optical light scattering qualitatively confirms the observations made by depth dependent microscopy. It provides an average over the thickness of the polymer. The black inner most ring of each pattern corresponds to the main beam from which no data is acquired. In these figures, isocontours of the scattered intensity are displayed in various shades of gray. The scattered intensity in all cases is a decreasing function of radial position. The scattering vector $\vec{q}$ ranges from 2.0 μm at the edge of the beam stop to 6.8 μm at the edge of the 2-D image. From a qualitative perspective, information about the shape of the droplet can be obtained from that of the scattering diagram. Thus in *Figure 8A* (σ_w = 2.6 kPa) we can infer that the droplets are nearly spherical. However, at the wall shear stress of σ_w = 15 kPa the pattern is (*Figure 8B*) best described by a two state model. Elongated strings along the z direction of a scattering pattern indicate polymer strings aligned in the flow direction of the actual material. Superimposed on this scattering pattern is an elliptical scattering pattern with long axis along the z direction; this indicates ellipsoidal droplets with long axis in the flow direction. Further increasing wall shear stress, we see first enhancement of string formation (*Figure 8C*, σ_w = 41 kPa) followed by a return to mildly deformed droplets (*Figure 8D*, σ_w = 68 kPa) and (*8E*, σ_w = 89 kPa). This progression follows that observed by the microscopy. The microscopy (*Figure 8*) and the optical light scattering (*Figure 8*) can be directly compared by matching the wall shear stress; for example *Figure 8C* corresponds approximately to the solid lines of (*Figure 8*) that have a wall shear stress of 10 kPa.

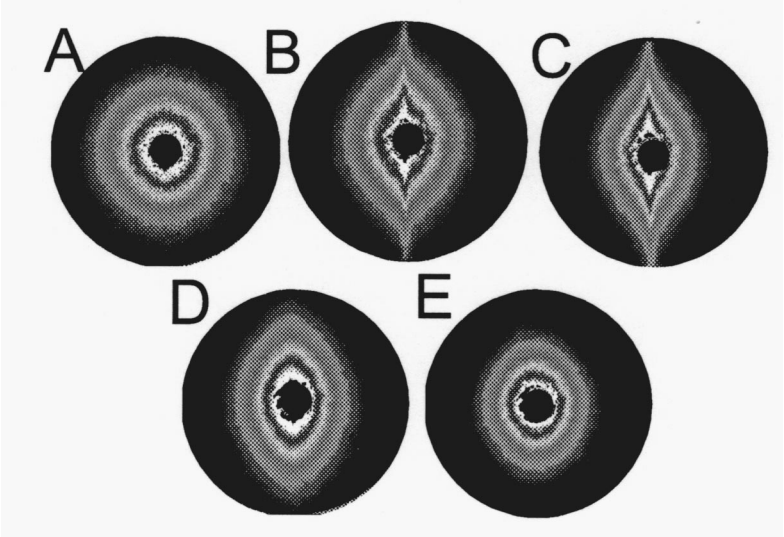

Fig. 8. Optical light scattering as a function of increasing wall shear stress. A: Ellipsoids σ_w = 2.6 kPa. B: Ellipsoids and strings σ_w = 15 kPa. C: σ_w = 41 kPa. D: Return to ellipsoids σ_w = 68 kPa. E: σ_w = 89 kPa.

The light scattering is sensitive to changes in size of the droplets. In the case where the scattering and microscopy indicate the presence of droplets only, we can estimate their size by fitting the data (in a slice along the q_z axis) to the Debye-Bueche equation as shown in *Figure 9*:

$$S(q) = \frac{S(0)}{(1 + \xi^2 q^2)^2} \tag{5}$$

where ξ is a correlation length. Using this approach, we find $\xi = 0.79 \pm 0.3$ μm for σ_w = 2.5 kPa and $\xi = 0.96 \pm 0.3$ μm for σ_w = 89 kPa in which the expanded uncertainty is derived from a fit to data. Thus the average size is even smaller at the low shear rate than at high shear rate.

DISCUSSION AND CONCLUSION

In this work, we see that droplet deformation and breakup can be visualized in-line under processing conditions in a measurable flow field. In the vicinity of the critical capillary number, strings are observed whose elongation greatly exceeds that seen in newtonian fluids. This result is consistent with the case where the elasticity of the matrix exceeds that of the droplet. The rheology on the individual blend components indicates that in the low stress regime, the normal force of the matrix does exceed that of the droplet when plotted as a function of shear stress. Shear stress (rather than shear rate) is the relevant variable for comparing the relative strengths of the normal forces because in the simple picture, shear stress is continuous across the

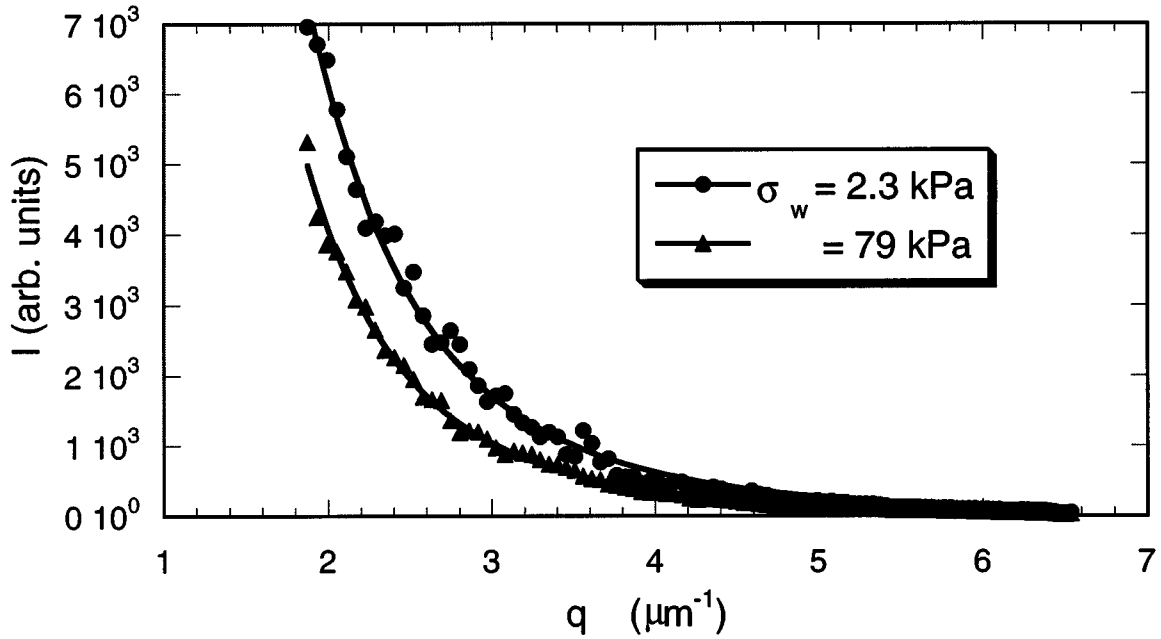

Fig. 9. Optical light scattering intensity in the q_z direction at the lowest and highest shear stresses, where ellipsoidal droplets only are observed. Relative expanded uncertainty in I is 10%, based on repeated measurements.

droplet-matrix interface. Elongated strings are observed to breakup into an irregular sequence of shorter and wider strings. Depth dependent microscopy indicates that shear stress is the controlling parameter for elongation and breakup; the morphology can transform from spheres to strings to broken strings by either increasing the flow rate at a fixed distance from the wall or by carrying out successive measurements at varying depths from the wall.

At higher shear stress typical of polymer processing, we see that droplet deformation is suppressed, even though $Ca/Ca_c \approx 10$. These results are consistent with earlier work which shows that the final droplet radius first decreases with increasing shear stress, but then remains constant or even increases with stronger shear stress. The rheology indicates that as shear stress increases, the droplet normal forces becomes increasingly large relative to the matrix. A partial explanation is that the normal forces retard the elongation of droplets, which is observed in the case where the elasticity of the droplet exceeds that of the matrix. In the high shear case, one would then expect to see droplets in the regions of high shear (near the wall) and in regions of low shear (at the mid-plane of the slit), and strings at intermediate distances. However, at high shear, we observe droplets at all distances. Further work is required to sort out the relative contributions to droplet morphology from elasticity, upstream breakup, and shear stress. It is likely that the effects that we visualize here are ubiquitous in polymer processing, hence continued investigation of the effects of normal forces and viscoelasticity is warranted.

ACKNOWLEDGMENT

We gratefully acknowledge the assistance of K. S. Hyun and C. C. Han.

REFERENCES

1. I. Manas-Zloczower and Z. Tadmor, *Mixing and Compounding of Polymers: Theory and Practice*, Hanser Publishers, New York (1994).
2. D. R. Paul and S. Newman, *Polymer Blends* Academic Press, New York (1978) .
3. T. J. Nelson and N. Subramanian, *Polymer International*, **32**, 343 (1993).
4. D. E. Kirkpatrick, J. K. McLemore and M. A. Wright, *J. Appl. Polym. Sci.*, **46**, 377 (1992).
5. H. E. H. Meijer, P. J. Lemstra and P. H. M. Elemans, *Makromolekulare Chemie-Macromolecular Symposia*, **16**, 113 (1988).
6. G. I. Taylor, *Proc. Roy. Soc. Lond. A*, **138**, 41 (1932).
7. S. Tomotika, *Proc. R. Soc. Lond.*, **A150**, 322 (1935).
8. G. I. Taylor, *Proc. Roy. Soc. Lond. A*, **146**, 501 (1934).
9. R. G. Cox, *J. Fluid Mech.*, **37**, 601 (1969).
10. F. D. Rumscheidt, Mason, S.G., *J. Coll. Interface Sci.*, **16**, 238 (1961).
11. H. P. Grace, *Chem. Eng. Commun.*, **14**, 225 (1982).
12. B. J. Bentley and L. G. Leal, *J. Fluid Mech.*, **167**, 219 (1986).
13. B. J. Bentley and L. G. Leal, *J. Fluid Mech.*, **167**, 241 (1986).
14. H. A. Stone, *Annual Review of Fluid Mechanics*, **26**, 65 (1994).
15. E. H. Meifer and J. M. H. Janssen, in *Mixing and Compounding of Polymers: Theory and Practice*, p. 86, I. Manas-Zloczower, and Z. Tadmor, eds., Hanser, New York (1994).
16. P. P. Varanasi, M. E. Ryan and P. Stroeve, *Industrial & Engineering Chemistry Research*, **33**, 1858 (1994).
17. J. J. Elmendorp and R. J. Maalcke, *Polym. Eng. Sci.*, **25**, 1041 (1985).
18. J. J. Elmendorp, *Polym. Eng. Sci.*, **26**, 418 (1986).
19. R. W. Flumerfelt, *Ind. Eng. Chem. Fundam.*, **11**, 312 (1972).
20. H. Vanoene, *J. Coll. Interface Sci.*, **40**, 448 (1972).
21. U. Sundararaj and C. W. Macosko, *Macromolecules*, **28**, 2647 (1995).
22. N. Chapleau and B. D. Favis, *Journal of Materials Science*, **30**, 142 (1995).
23. P. Cigana, B. D. Favis, C. Albert and T. VuKhanh, *Macromolecules*, **30**, 4163 (1997).
24. J. J. Elmendorp and A. K. Vandervegt, *Polym. Eng. Sci.*, **26**, 1332 (1986).
25. B. D. Favis and J. P. Chalifoux, *Polym. Eng. Sci.*, **27**, 1591 (1987).
26. B. D. Favis, *Polymer*, **35**, 1552 (1994).
27. P. G. Ghodgaonkar and U. Sundararaj, *Polym. Eng. Sci.*, **36**, 1656 (1996).
28. R. Gonzalez Nunez, B. D. Favis and P. J. Carreau, *Polym. Eng. Sci.*, **33**, 851 (1993).
29. R. Gonzalez Nunez, C. Fong, B. D. Favis and D. DeKee, *J. Appl. Polym. Sci.*, **62**, 1627 (1996).
30. N. Mekhilef, B. D. Favis and P. J. Carreau, *J. Polym. Sci., Polym. Phys.*, **35**, 293 (1997).
31. C. E. Scott and C. W. Macosko, *Polym. Eng. Sci.*, **35**, 1938 (1995).
32. U. Sundararaj, C. W. Macosko, R. J. Rolando and H. T. Chan, *Polym. Eng. Sci.*, **32**, 1814 (1992).
33. U. Sundararaj, C. W. Macosko and C. K. Shih, *Polym. Eng. Sci.*, **36**, 1769 (1996).
34. C. G. Gogos, M. Esseghir, D. B. Todd and D. W. Yu, *Macromolecular Symposia*, **101**, 185 (1996).
35. S. L. Sakellarides and A. J. McHugh, *Polym. Eng. Sci.*, **27**, 1662 (1987).
36. K. Sondergaard and J. Lyngaae-Jorgensen, *Rheo-Physics of Multiphase Polymer Systems*, Technomic Publishing Company, Lancaster, Pa. (1995).
37. N. G. Remediakis, R. A. Weiss and M. T. Shaw, *Rubber Chemistry and Technology*, **70**, 71 (1997).
38. S. Kim, J. W. Yu and C. C. Han, *Rev. Sci. Inst.*, **67**, 3940 (1996).
39. S. Kim, E. K. Hobbie, J. W. Yu and C. C. Han, *Macromolecules*, **30**, 8245 (1997).
40. J. W. Yu, J. F. Douglas, E. K. Hobbie, S. Kim and C. C. Han, *Phys. Rev. Lett.*, **78**, 2664 (1997).
41. S. Li, K. B. Migler, E. K. Hobbie, H. Kramer, C. C. Han and E. J. Amis, *J. Polym. Sci., Polym. Phys.*, **35**, 2935 (1997).
42. Certain commercial equipment, instruments, or materials are identified in this paper in order to adequately specify the experimental conditions. Such identification does not imply recommendation by the National Institute of Standards and Technology, nor does it imply that the materials are necessarily the best available for the purpose.
43. C. W. Macosko, *Rheology: Principles, Measurements, and Applications*, Vch, New York (1994).
44. C. W. Macosko and W. M. Davis, *Rheol. Acta*, **13**, 814 (1974).
45. E. K. Hobbie and K. B. Migler, *Phys. Rev. Lett.*, **82**, 5393 (1999).